Journal of The Electrochemical Society

OPEN ACCESS

Coordination-Controlled Electrodeposition of Palladium/Copper Thin Films onto a Pyridine-Terminated Self-Assembled Monolayer

To cite this article: Zhen Yao *et al* 2022 *J. Electrochem. Soc.* **169** 112515

View the article online for updates and enhancements.

This content was downloaded from IP address 138.251.135.69 on 24/11/2022 at 09:49

Journal of The Electrochemical Society, 2022 **169** 112515

Coordination-Controlled Electrodeposition of Palladium/Copper Thin Films onto a Pyridine-Terminated Self-Assembled Monolayer

Zhen Yao,[a,z] Aaron B. Naden, Richard T. Baker, and Manfred Buck[*,z]

EaStCHEM School of Chemistry, University of St Andrews, North Haugh, St Andrews, KY16 9ST, United Kingdom

A scheme for the electrodeposition of ultrathin bimetallic layers on top of a self-assembled monolayer (SAM) is investigated which combines the deposition of one metal (Pd) coordinated to a functionalized SAM (3-(4-pyridine-4-yl-phenyl)-propane-1-thiol, PyP3) on Au/mica with another metal (Cu) from the bulk electrolyte. The coordination-controlled electrodeposition (CCED) is a four-phase process comprising (i) Pd^{2+} coordination to the terminal pyridine units of the SAM, (ii) reduction of Pd and nanoparticle formation, (iii) formation of an intermixed shell of Pd and Cu, and (iv) deposition of bulk Cu. Chronoamperometry reveals a fast nucleation phase where Pd nanoparticles form within a few milliseconds and seed the Cu deposition. The Pd-Cu core-shell nature of deposited nanoparticles is confirmed by transmission electron microscopy (TEM). Harnessing the selective coordination of Pd^{2+} to PyP3, a one-pot procedure is further developed using electrolytes containing both Pd^{2+} and Cu^{2+} ions. Thus simplifying complexation and reduction, continuous Pd/Cu films are obtained in a multistep process as verified by scanning tunneling microscopy (STM). With a percolation threshold below 3 nm, CCED, as a SAM-controlled deposition strategy, offers an avenue for generation of ultrathin films.

© 2022 The Author(s). Published on behalf of The Electrochemical Society by IOP Publishing Limited. This is an open access article distributed under the terms of the Creative Commons Attribution 4.0 License (CC BY, http://creativecommons.org/licenses/by/4.0/), which permits unrestricted reuse of the work in any medium, provided the original work is properly cited. [DOI: 10.1149/1945-7111/aca17e]

Manuscript submitted August 15, 2022; revised manuscript received October 6, 2022. Published November 23, 2022. *This paper is part of the JES Focus Issue on Nucleation and Growth: Measurements, Processes, and Materials.*

Supplementary material for this article is available online

Control of interfacial charge transfer, chemical functionalization of surfaces, tuning of interfacial energies, and the availability of patterning techniques down to the nanometer scale is a combination of features which makes SAMs attractive templates for electrodeposition schemes, including the lift-off and transfer of the deposited films or structures to foreign substrates. Compared to the well-established approach using chemically inert SAMs,[1–7] functionalised layers bearing metal coordinating moieties change the paradigm from defect-based electrodeposition to deposition controlled by molecular properties. The different mechanism not only confines deposition to on top of the SAM as first reported by Kolb et al.[8–10] but the level of control over the deposition process offers new prospects for the design of materials as illustrated by the tuning of electronic properties,[11–16] generation of SAM/metal hybrid structures,[17] control of catalytic activity,[12,18,19] the epitaxial growth of Cu films on a cysteine modified Au surface,[20] or the generation of bimetallic nanostructures.[21]

Coordination-controlled electrodeposition (CCED) can be accomplished in different ways and the ones employed in the work presented here are illustrated in Fig. 1. Building on the original work by Kolb and coworkers,[8,9] which was performed with metal coordinated to a SAM of mercaptopyridine thiol in an electrochemically inert electrolyte, deposition is performed with a metal present in the bulk electrolyte. This is afforded by SAMs which are structurally sufficiently robust to avoid the problem of defect-mediated deposition from the bulk electrolyte in parallel to CCED.[22–24] Key steps of the deposition scheme are the coordination of metal ions (A^{n+}) to the SAM (step i), Pd^{2+} in the present study, followed by the formation of nanoparticles upon electrochemical reduction of the coordinated ions and diffusion of the metal atoms at the SAM/electrolyte interface (ii). The nanoparticles, thus formed on top of the SAM by the two-dimensional (2-D) deposition process, act as seeds for the electrodeposition of species B (here Cu) from the bulk (3-D) electrolyte (iii). It is noted that the complexation step is carried out without applying a potential and can be done either ex-situ in a setup separate from the electrochemical cell (procedure 1) or in situ in the electrochemical cell with the coordinating metal ions A^{n+} also present in the bulk electrolyte (procedure 2). This makes multiple coordination/deposition cycles straightforward and thus increases particle density up to their coalescence and formation of continuous layers. Through the combination of 2-D and 3-D deposition, additional degrees of freedom in the composition and morphology of bimetallic deposition become available, in particular, if metals are used which, like Cu and Pd differ in their propensity to coordinate to the SAM.[21]

The work presented here is a detailed investigation of Pd/Cu CCED on PyP3 SAM functionalized Au(111) electrodes directed towards the generation of ultrathin layers. Aiming for continuous layers, different preparation protocols are compared including the simplification of the coordination and reduction steps to a one-pot procedure. The morphology of the deposits is characterized by scanning tunnelling microscopy (STM). The lift-off and transfer of the ultrathin metal films are accomplished, and structural and chemical information on the Pd/Cu nanolayers is obtained by scanning transmission electron microscopy (STEM) combined with energy-dispersive X-ray (EDX) spectroscopy.

Experimental

Materials and sample preparation.—Potassium hydroxide (Fluka, 99.99%), palladium sulfate (Sigma-Aldrich, 98%), copper sulfate pentahydrate (Aldrich, 99.999%), potassium chloride (Fluka, ⩾99.5%), sulfuric acid (Sigma-Aldrich, 99.999%), and absolute ethanol (AnalaR NORMAPUR, 100%) were used as received. Platinum wire (0.25 mm diameter) and copper wire (0.25 mm diameter) used as counter and reference electrodes were purchased from ADVENT Research Materials. Polyvinyl alcohol (87%–89% hydrolysed, high molecular weight) for the lift-off and transfer of the deposited metal layers was used as received from Alfa Aesar.

Substrates, Au(111)/mica (300 nm thick) were purchased from Georg Albert PVD (Silz, Germany) and stored in vacuum and flame-annealed prior to thiol exposure. The synthesis of PyP3 has been described previously.[25] Samples were prepared by immersing the substrates in a solution of 100 μM PyP3 in a basic ethanol solution (KOH, pH $\sim$ 8.0) at elevated temperature ($\sim$343 K) overnight ($\sim$15 h),[25] followed by a thorough rinse with EtOH and drying in a stream of N_2 gas.

Pd/Cu deposition.—Deposition was performed in a homemade cell with a hanging meniscus configuration. Different types of

*Electrochemical Society Member.
[a]Present address: Fakultät für Physik, Universität Bielefeld, Universitätsstr. 25, 33615 Bielefeld, Germany.
[z]E-mail: zhen.yao@uni-bielefeld.de; mb45@st-andrews.ac.uk

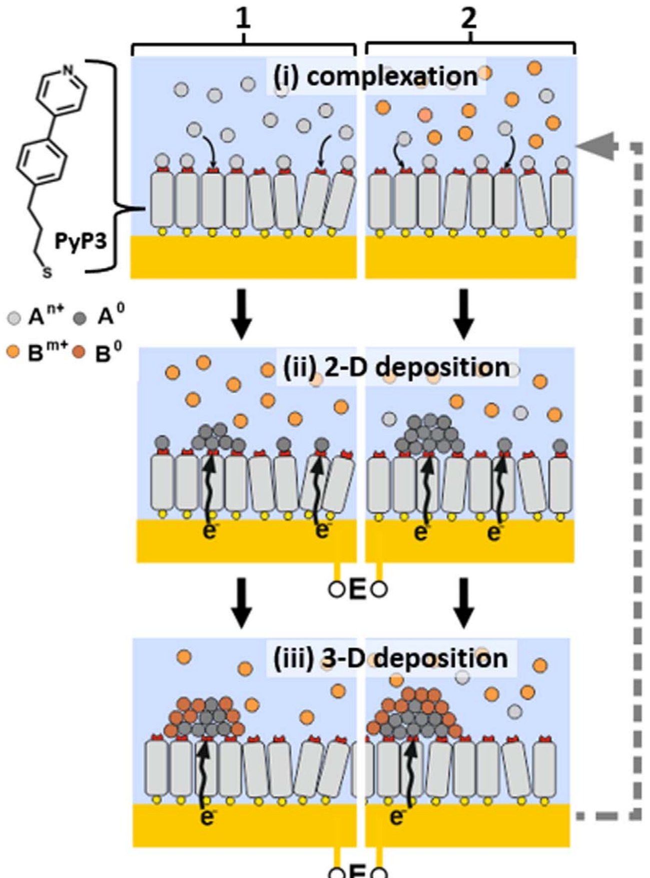

Figure 1. Illustration of steps involved in bimetallic CCED on a SAM-modified electrode. After one metal is coordinated to the SAM (i), the electrodeposition is carried out in the presence of a second metal in the bulk electrolyte. Starting with the reduction of the coordinated metal (ii), the deposition from the bulk electrolyte follows (iii) with both processes overlapping. Complexation and deposition can be performed either in separate setups (1) with the bulk electrolyte containing only one species or in a one-pot setup (2) using an electrolyte containing both species. As indicated by the dashed arrow, the sequence can be repeated to increase coverage and generate continuous layers. The structure of the pyridine-terminated SAM molecule used in this work is also shown.

electrolytes were used for the electrochemical deposition. Acidic copper sulfate solution (5 mM $CuSO_4$/50 mM H_2SO_4) was used throughout the experiments. KCl at 50 mM concentration was added in experiments where the influence of chloride on the deposition process was studied.

For the ex situ Pd complexation (procedure 1, Fig. 1) samples were immersed in a 100 μM $PdSO_4$/50 mM H_2SO_4 solution for 30 min. For the in situ complexation in the one-pot procedure (2 in Fig. 1) $PdSO_4$ or, if KCl was present, $PdCl_2$ was added to the Cu solutions at concentrations of 5 μmol or 50 μmol, depending on the experiment, as specified in the figure captions. Pd complexation was done without potential control. Cu wires were used as pseudoreference and counter electrodes for Pd/Cu deposition. The potentials reported are referenced to the saturated calomel electrode (SCE) with +0.03 V as the difference between Cu and SCE at a concentration of 5 mM.

Starting from the open circuit potential, pulsed deposition was employed. Deposition potentials, pulse duration, and the number of pulses employed are specified in the figure captions. Unless stated otherwise bulk Cu was dissolved by applying +0.13 V for at least 500 ms. Samples were removed from the cell immediately after deposition and blown dry with N_2. They were then rinsed with deionised (DI) water and again dried with N_2 before STM characterisation.

STM characterisation.—Measurements were performed under ambient conditions using a PicoPlus STM (Molecular Imaging) and PicoScan 5.3.3 software. Images were acquired in constant current mode with tips mechanically cut from a 0.25 mm diameter Pt/Ir wire (80:20, hard-tempered, Advent Research Material Ltd.). Imaging conditions and stability were substantially dependent on the details of the deposition. Since Pd and Pd/Cu metal nanoparticles adhere weakly to pyridine-terminated SAMs[14,23,24] isolated particles are easily removed by attachment to the tip. Therefore, the tip-to-sample distance was maximized by applying a high sample bias of ±1–1.5 V and a low current (<5 pA). For samples with aggregated particles or continuous layers, imaging is less critical, thus allowing for a lower bias of a few hundred mV and higher currents of a few tens of pA. Imaging parameters for the figures shown are provided in Table S1 of the supporting information. Images were evaluated using WSxM software.[26] For selected images with particle numbers in the range of 300 to 1000, depending on coverage, size distributions were manually determined using ImageJ software.[27]

STEM characterisation.—The composition and morphology of Pd/Cu nanoparticles were also analyzed using a Titan Themis scanning transmission electron microscope (STEM) operated at 200 kV. The two-dimensional maps of the elemental composition were obtained by energy-dispersive X-ray (EDX) spectroscopy. The sample preparation is described in the Supporting Information.

Results and Discussion

Pd promoted Cu deposition.—Under the acidic conditions employed here, Pd^{2+} coordinates to the PyP3 SAM whereas Cu^{2+} does not. Accordingly, the process can be formally split into the 2-D deposition of Pd and the 3-D deposition of Cu. In order to study the effect of Pd on the Cu deposition from the bulk electrolyte, procedure 1 (see Fig. 1a) was employed by exposing a PyP3-SAM/Au sample to an acidic Pd^{2+} solution for 30 min prior to the deposition of Cu. As evidenced by the cyclic voltammograms (CVs) and the chronoamperograms depicted in Fig. 2, the Pd complexation fundamentally alters the deposition process. The CVs (Fig. 2a) are in line with previous experiments performed with lower Cu concentration.[21] The pristine PyP3 SAM passivates the electrode (blue curve), whereas an increase in current more negative than –0.13 V for the Pd^{2+} complexed SAM (red curve) indicates the deposition of Cu from the bulk electrolyte, which is again dissolved during the anodic sweep.

Further insight is gained by chronoamperometric measurements as displayed in Fig. 2b, which shows I-t curves for a potential switched from the open circuit potential to −0.37 V. At this more negative potential than covered by the CVs, the passivating effect of the pristine PyP3 SAM breaks down. The current increases gradually until about 450 ms before becoming mass transport limited, which is a shape characteristic of a hindered nucleation and growth process and typical for metal deposition mediated by defects in the SAM.[3,6] The current of the Pd-modified SAM yields a pronouncedly different time dependence and, thus, reflects a very different deposition mechanism. When the potential is switched to –0.37 V, the current immediately jumps to much higher values compared to the pristine PyP3 SAM, decays within the first few ms as seen from the inset of Fig. 2b and passes a maximum at about 20 ms before becoming limited by diffusion.

The differences between the deposition processes are also evident from STM images, which show in a comparison (Fig. 3) the Pd modified SAM (left series) and the pristine SAM (right series) together with illustrations of the processes taking place.

After a deposition time of 25 ms a significant difference in surface morphology is observed. At this initial stage, the Pd^{2+}-complexed SAM sample is already covered with isolated particles (Fig. 3a), whereas the pristine PyP3 SAM surface is essentially free of particles (Fig. 3d). This is in line with the very different course and magnitude of the currents seen in the chronoamperograms. The high current for

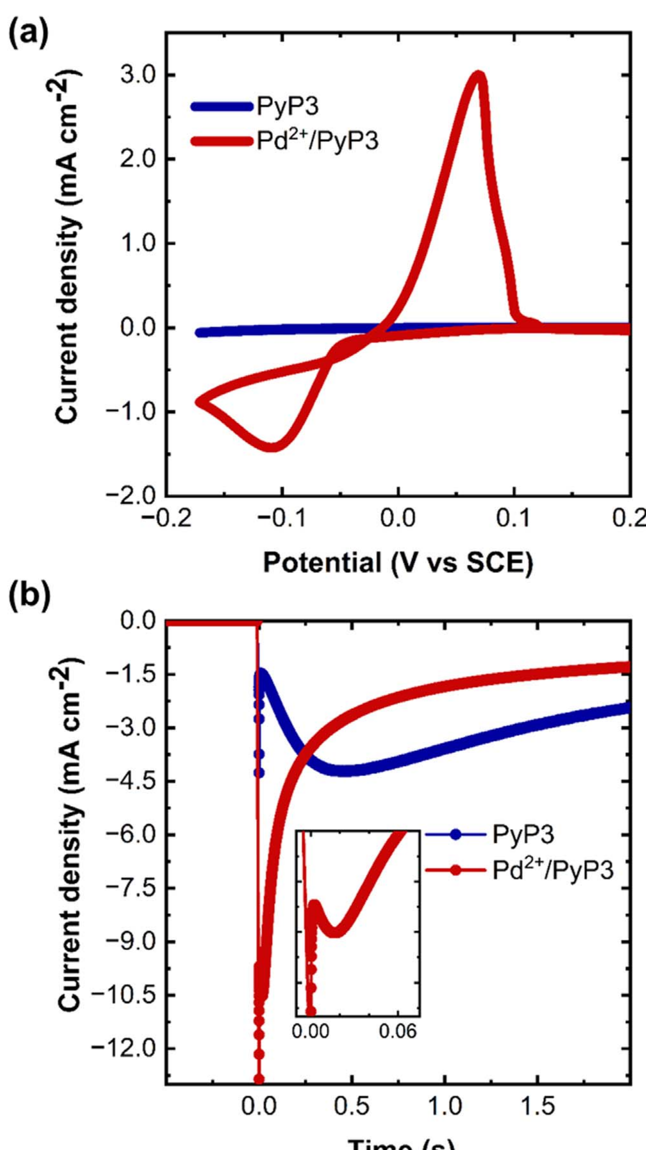

Figure 2. Comparison of Cu deposition on PyP3 SAM on Au(111)/mica without (blue curves) and with (red) Pd^{2+} coordination. (a) Cyclic voltammograms. Scan rate 10 mV s^{-1}. (b) I-t curves with inset showing the initial 60 ms of the deposition for the Pd^{2+}/PyP3 SAM. At t = 0 the potential is switched from OCP (+0.28 V and +0.40 V without and with Pd coordination, respectively) to −0.37 V. The Pd^{2+}-complexation was performed ex-situ by immersing the sample in 100 μM $PdSO_4$/50 mM H_2SO_4 for 30 min. Electrolyte: 5 mM $CuSO_4$/50 mM H_2SO_4.

the Pd^{2+}/PyP3 system during the first few ms is determined by the reduction of the coordinated Pd^{2+}. Indicated by path 1 in the illustrations of Fig. 3a, electron tunneling across the SAM is the rate-determining factor at this stage. The absence of particles on the PyP3 sample proves that path 4, the reduction of Cu^{2+} ions at the SAM/electrolyte interface does not play a role. Obviously, the electronic coupling of the hydrated Cu^{2+} ions to the SAM is negligible compared to that of the coordinated Pd^{2+}. Following reduction, the Pd atoms diffuse on the SAM, nucleate, and coalesce to form nanoparticles. This opens the sequence of pathways 2 and 3 for Cu deposition. It is noted that electron tunneling from the Pd particles to the hydrated Cu^{2+} ions (3) quickly becomes the rate-limiting step as the rate of tunneling across the SAM (2) increases due to the high density of states in the metallic Pd nanoparticles, i.e., they behave like a metal electrode.[28] However, since this configuration represents a double tunnel junction, the nanoparticles also have to reach a minimum size in order for the Coulomb barrier to be overcome. Comparing the Coulomb charging energy[27] with the potentiostatic energy $e^2/(\pi d^2 C) \approx eE$, where d denotes the particle size, C the double layer capacitance and E the deposition potential, a value for d in the range of 1 nm is estimated using a typical value of C for a metal surface (20 μF cm^{-2}) at the negative deposition potentials of a few hundred mV.[29] The shallow minimum at ∼2 ms and subsequent increase in current up to 25 ms seen in the I-t curve of Fig. 2b suggest that there is an overlap between the phase where Pd still nucleates and Cu deposition has already started, which explains the Pd/Cu alloy formation before bulk Cu is deposited.[21] In the STM images no selectivity in the location of particles was observed, i.e., no preferred nucleation occurred at intrinsic substrate defects like edges of the substrate or vacancy islands compared to flat terraces. Whether defects in the SAM such as domain boundaries or other packing faults act as traps for diffusing Pd atoms and, thus, nucleation sites cannot be determined at present since after deposition the SAM itself cannot be imaged at molecular resolution. The main reason for this is the lower resolution of the tip, which arises from the occasional pick-up of weakly adhering isolated particles deposited on top of the SAM.

Extending the deposition time to 1500 ms leads to the formation of a layer of connected particles on Pd^{2+}/PyP3 (Fig. 3b) while, in contrast, only a few isolated and rather large particles are formed on the pristine PyP3 SAM sample (Fig. 3e) due to defect-mediated deposition represented by pathway 5 indicated in the sketch to Fig. 3d. However, also for the Pd^{2+}/PyP3 SAM some larger particles are observed. With diameters of 10–20 nm and heights of 5–8 nm they stick out from the background of the smaller ones which are 2–3 nm high. This suggests that at this extended deposition time the Pd-promoted deposition of Cu on top of the SAM is paralleled by some defect-mediated deposition. We return to this point in the context of multipulse deposition and just note at this point that the extent to which this defect-mediated pathway might contribute depends on the combination of deposition parameters such as metal ion concentration, potential, and pulse duration. For example, more cathodic potentials will require shorter times as evidenced by the comparison of Cu deposition on aPyP3 sample at different potentials. As shown in Fig. S1 the deposition of monoatomic islands of Cu buried at the SAM/Au interface is already seen after 25 ms at –0.6 V but not at –0.37 V.

Most of the material deposited onto the Pd^{2+}/PyP3 SAM within 1500 ms is bulk Cu which can be straightforwardly dissolved by exposing the sample to aerated 50 mM H_2SO_4. After this treatment the large particles on the Pd^{2+}/PyP3 sample have disappeared, leaving the surface covered with a layer of nanoparticles which are mostly isolated (Fig. 3c). They have a diameter of 4–8 nm and an average height of about 2 nm. In comparison, the acid treatment of the Pd-free PyP3 looks like that of a pristine SAM (Fig. 3f). Comparing the Pd^{2+}/PyP3 sample after 25 ms Cu deposition (Fig. 3a) with the one after 1500 ms and Cu dissolution (Fig. 3c), the particle density of the latter is much higher. It is also much higher compared to Pd deposition when no Cu is present in the electrolyte.[21,24] This proves that, even though Pd deposition is a prerequisite for Cu deposition, both processes overlap beyond the initial 25 ms, leading to Pd/Cu alloy formation in which Cu is more noble than bulk Cu and, thus, more resistant to oxidative etching. This is in full agreement with XPS results where chemically different Pd states are seen in the Pd-promoted Cu deposition on PyP3 SAMs.[21]

Formation of ultrathin continuous layers.—As shown in the previous section, particles of sub-3 nm height can be easily generated via Pd/Cu alloy formation. This offers the perspective of generating ultrathin metal layers and significantly reducing the percolation threshold compared to layers which are generated by defect-based deposition. However, this requires an increase in the particle density beyond what is feasible with a single complexation/deposition sequence. Analogous to Pd-only deposition,[9,11,24] the particle coverage can be increased stepwise by multiple

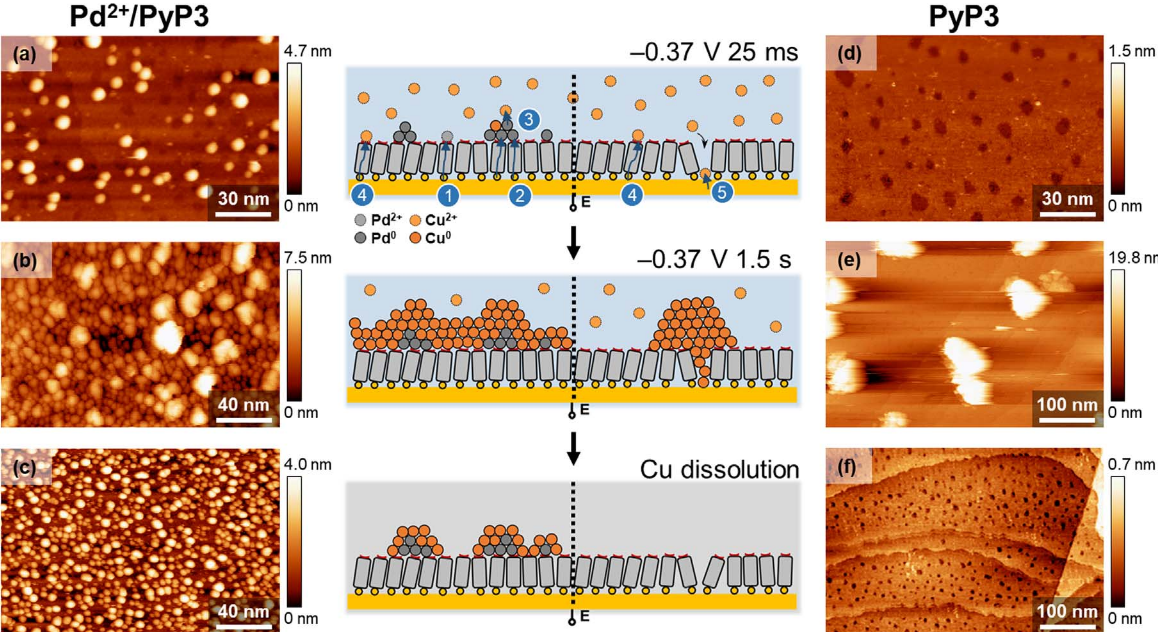

Figure 3. STM images and corresponding illustrations of Cu electrodeposition onto (a)–(c) ex situ Pd^{2+}-complexed PyP3 SAM and (d)–(e) pristine PyP3 SAM at a potential of –0.37 V (vs SCE) for 25 ms (a), (d), 1500 ms (b), (e) and after the dissolution of bulk Cu in aerated 50 mM H_2SO_4 (c), (f).

complexation-reduction cycles according to procedure 1 (see Fig. S2 in SI). However, this is cumbersome and a more simple approach as outlined by procedure 2 in Fig. 1b is desirable where, similar to the Pd metallization of a SAM by hydrogen,[23] reduction of Pd^{2+}, complexation and deposition is carried out in a single setup using a mixture of both metal ions. Aiming for ultrathin layers, a boundary condition for this procedure is that the Pd deposition should be limited to the 2-D layer of coordinated ions. Therefore, the concentration of Pd^{2+} in the electrolyte has to be much lower than that of Cu^{2+}, thus making direct Pd deposition from the bulk electrolyte negligible.

Following procedure 1 the starting point is a PyP3 SAM with a saturated Pd^{2+} coverage prepared by immersing the sample in a 100 μM $PdSO_4$/50 mM H_2SO_4 solution for 30 min before mounting it onto the electrochemical setup with a mixed 5 μM Pd^{2+}/50 mM Cu^{2+} electrolyte. With the intention to shift the onset of Cu deposition to shorter times and, thus, create smaller particles, a more negative potential of –0.57 V compared to the above experiments is applied for 25 ms. Then the potential is switched to +0.13 V to strip the Pd/Cu deposit of any bulk Cu. To replenish the SAM with Pd^{2+} the sample remains exposed to the electrolyte for 15 min without applying a potential, after which the deposition/stripping sequence is repeated. After two pulses (Fig. 4a), some Pd/Cu particles are deposited on the surface but the density of $\sim 8 \times 10^3$ per μm^2 is quite low. It increases with the number of times the complexation/deposition sequence is performed. After six pulses (Fig. 4b), a continuous layer is formed with a thickness below 3 nm. The root-mean-square (rms) roughness of this layer is 0.65 nm.

In our efforts to minimize the thickness of the layers we also looked into the effect chloride might have on the nucleation and growth behaviour of the Pd/Cu particles as other studies have shown that Cl^- affects the Cu electrodeposition process.[30–34] Both chemical and structural arguments have been put forward, and accelerating effects at low, or inhibiting effects at high, Cl^- concentrations have been found.[32,35] The present case is even more complex due to the different surface - a SAM instead of metal surfaces - and the involvement of Pd where the reduction of the coordinated Pd^{2+}, diffusion and nucleation of Pd^0 could also be affected by a change in the ratio of water to chloride ligands.[36] Comparing I-t curves for the Pd/Cu deposition with and without Cl^- (Fig. 4f), the addition of 50 mM Cl^- has a clear accelerating effect. The initial current is higher and, contrasting the shape of the curve measured without Cl^-, only a monotonous decay of the signal is observed. This suggests a shift of the onset of Cu deposition to shorter times and, thus, a larger overlap with the Pd reduction and nucleation. STM images like the one seen in Fig. 4c show an increased density of particles of $\sim 12 \times 10^3$ per μm^2, which can be accounted for by a shift of the critical size of Pd nuclei to smaller sizes and/or their earlier stabilization by Cu deposition. Correspondingly, a dense layer is formed after five pulses (Fig. 4d). The kinetics altered by Cl^- also affects the morphology of the layer, thus yielding slightly thinner layers as seen from the comparison of the height profiles in Fig. 4e and a smaller rms roughness of $\sim$0.45 nm. Another notable feature of the images and height profiles is that, in agreement with results for layers prepared by protocol 1 (Fig. S2), the average height, diameter and size distribution of the particles are not substantially affected by increasing the number of pulses but the particle density increases. Similarly, the size distribution of the particles does not significantly change (Fig. S3). This indicates that freshly generated Pd atoms preferentially form new clusters rather than being incorporated into existing particles. This is analogous to the case of Pd deposition without Cu.[24] Also for Pd/Cu there seems to be a significant barrier for the Pd atoms to attach to existing particles, thus favoring the formation of new Pd seeds.

The experiments shown in Fig. 4 demonstrate that the one-pot complexation/deposition is a suitable protocol to increase the coverage up to continuous layers. Also incorporating the first complexation step into the sequence of depositions, the evolution of the Pd/Cu deposition from a chloride-containing electrolyte over 15 pulses is shown in Fig. 5. Compared to the experiment shown in Fig. 4, a higher concentration of 50 μM Pd^{2+} solution was chosen as a tradeoff between a reduction in the length of the experiment by shortening the complexation time and ensuring that in the subsequent deposition only the coordinated Pd is reduced but deposition of Pd from the bulk electrolyte is negligible compared to the deposition of Cu as illustrated by the STM images shown in Fig. S4. Albeit we have not yet studied the complexation kinetics of the PyP3 SAM, it is reasonable to assume that, based on literature data for Pd^{2+} complexation of mercaptopyridine SAMs,[37] after 1 min the Pd^{2+} coverage has not reached the saturation value. This should affect the particle density and, therefore, require more complexation/deposition cycles to achieve a closed Pd/Cu layer compared to the long immersion times applied in the experiments described above.

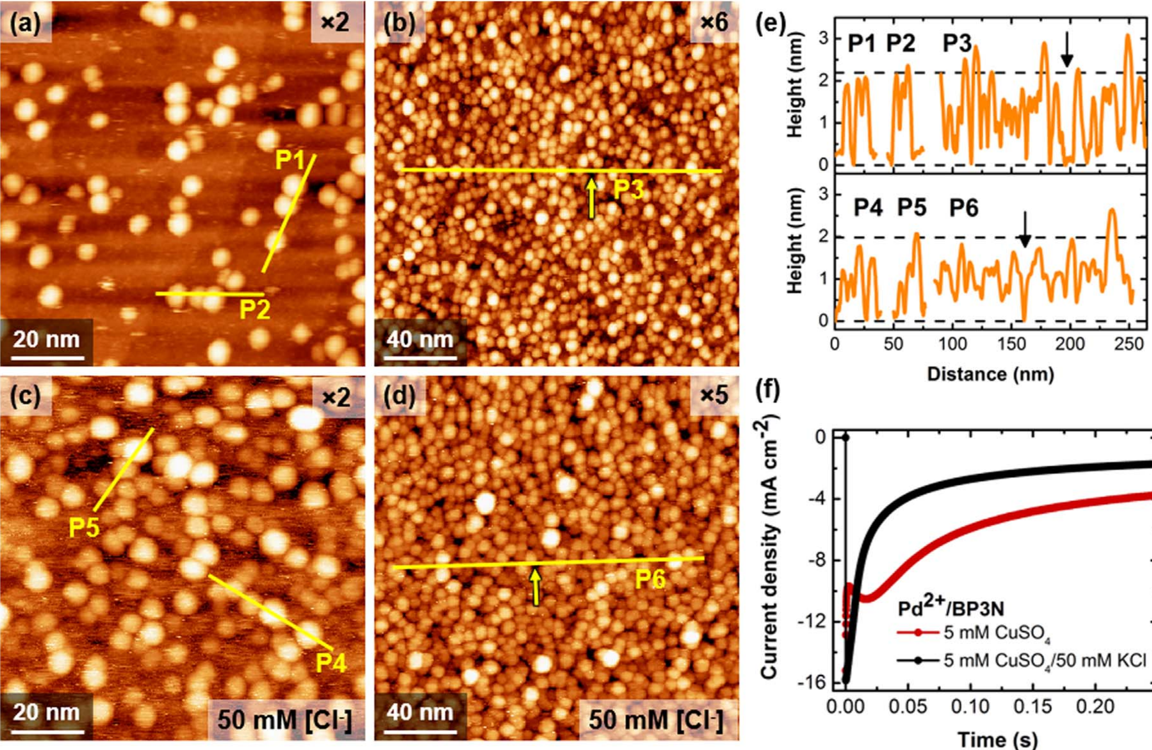

Figure 4. (a)–(d) STM images of Pd/Cu nanoparticles deposited onto Pd^{2+}/PyP3 SAMs in a chloride-free (a), (b) and chloride containing acidic Pd^{2+}/Cu^{2+} electrolyte (c), (d). Pulsed deposition (–0.57 V, 25 ms) was employed, and the number of pulses applied is indicated in the images. Each deposition pulse was followed by the dissolution of bulk Cu at +0.13 V for 500 ms. The initial complexation was carried out ex-situ, subsequently in situ for 15 min with 5 μM Pd^{2+} present in the Cu electrolyte. (e) Height profiles along the lines shown in images (a)–(d). Arrows in (b) and (d) point to defects in the layer where the underlying SAM is exposed, thus, serving as reference points for determining the thickness of the layer. (f) I–t curves for Cu deposition onto Pd^{2+}/PyP3 SAM with chloride present in the electrolyte (black curve) or absent (red curve). Deposition potential: –0.37 V. Cu electrolyte also contains 5 μM $PdSO_4$.

However, comparison of the data of Figs. 4 and 5 gives a somewhat different picture as a significant difference in coverage is observed during the first few pulses only.

After one pulse (Fig. 5a), the particle density of about 200 particles μm^{-2} is very low, even though this has to be considered a lower limit as we cannot exclude that due to their weak adhesion, some particles are lifted off as evidenced by the appearance of fractions of particles arising from their lift off during imaging. Even after the three pulses (Fig. 5c) the coverage is still lower than for the longer exposure after two pulses (Fig. 4c). However, with increasing particle density the generation of new particles seems to accelerate as after 5 pulses a continuous layer has formed albeit not as smooth (RMS roughness ~1 nm) as the corresponding one shown in Fig. 4d. Apart from filling of defects, additional cycles do not change the overall thickness of about 3 nm and roughness of the layer, indicating that Pd deposition is via complexation and that direct deposition from the bulk electrolyte does not play a noticeable role. However, the size of the particles has increased slightly and the particles look more facetted. The cause of the latter remains to be established and we can only speculate at present that this annealing effect arises from the repeated switch of potentials.

Another interesting point is whether, like for a PyP3 SAM without Pd complexation (Fig. S1a), defect-mediated Cu deposition can also play a role in the CCED scheme. Imaging after one pulse (Fig. 5b) there is no indication of substantial defect-mediated deposition. Noting that, for unknown reasons, imaging at molecular resolution is challenging for pyridine SAMs to which Pd has been coordinated,[8,24] protrusions reminiscent of molecules are seen with some occasional local order, albeit distances other than the 5 Å intermolecular distance of the pristine SAM are also present. This suggests that the complexation/deposition has an effect on the order of the SAM.

In contrast to the single pulse deposition where particles are sufficiently far apart to scan a SAM area free of particles, a different approach has to be taken for higher coverages. Harnessing the weak adhesion of the particles located on top of the SAM, they are removed by scanning the tip close to the surface, i.e. lower bias and larger current compared to imaging conditions. This was done from three pulses onward (Figs. 5d, 5f, 5h). After three pulses there is still no clear sign of deposition other than the nanoparticles on top of the SAM but stable islands together with vacancy islands in the substrate are clearly seen after 5 and 15 pulses. As seen from the line profiles the islands are of monoatomic height and, like the islands observed for PyP3 SAM (Fig. S1a), are interpreted as Cu deposited at defects in the SAM and located at the SAM/substrate interface.[38] Since the presence of islands seems to be correlated with the number of pulses it is reasonable to assume that the complexation and/or presence of the nanoparticles affects the structure of the SAMs and, thus, increases the likelihood of defect-mediated deposition from the bulk electrolyte. To what extent these buried metal islands can affect the CCED is unclear at present. We suggest that they affect the nucleation of the Pd by taking into account that the PyP3 molecules on top of the buried metal islands stick out from the surrounding SAM. The pyridine units now being more exposed, they represent preferential nucleation sites for the reduced Pd diffusing at the SAM/electrolyte interface. Support for this model comes from a recent computational study which found a preference of the Pd to sit in between rather than on top of the pyridine rings.[14] While this model is tentative it would explain the larger, more protruding particles seen in Figs. 5e and 5g as well as the difference in the number of larger particles and breadth of particle distribution compared to differently prepared samples like the one shown in Fig. 4d.

Transfer and TEM analysis.—So far, the characterization of metal structures deposited onto SAMs by either CCED[11,21,23,24,39] or defect-mediated deposition[3,6] has been based on a number of microscopies (SEM, AFM, and STM) and electron spectroscopies

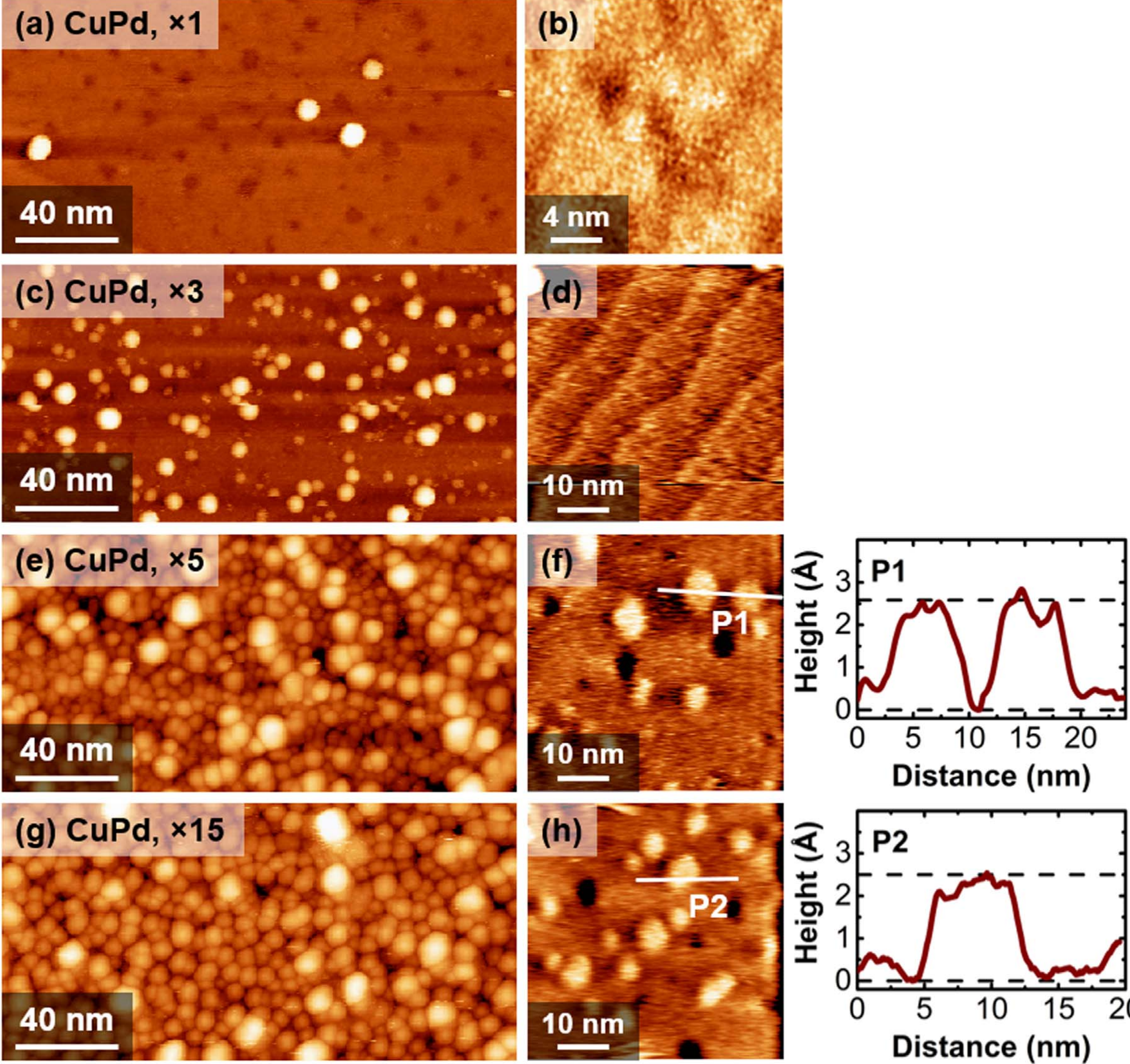

Figure 5. STM images and height profiles of Pd/Cu CCED onto BP3N SAM. Cu electrolyte contains 50 mM KCl and 50 μM $PdSO_4$. Each deposition cycle includes an in situ Pd complexation for 1 min. Deposition and bulk Cu dissolution were –0.57 V/25 ms and +0.13 V/2 s, respectively. (b) SAM layer after a single deposition cycle. (d)(f)(h) show the SAM surface after removing Pd/Cu nanoparticles. Particles are removed by scanning the 50 × 50 nm^2 with the set point at 0.01 V and 0.1 nA.

(XPS, UPS) but any information about the internal structure of the deposits has been limited. Only recently, X-ray diffraction was applied to Cu films of thickness in the 100 nm range, which were epitaxially grown on Au modified by a cysteine SAM.[20] With the possibility to generate continuous layers, in combination with the weak adhesion between metal layer and SAM, the possibility of lift-off and transfer onto a foreign substrate opens up (see SI for procedure), thus making the ultrathin Pd/Cu layers accessible to structural and chemical characterisation by the suite of TEM based methods as illustrated by Fig. 6. We note at this point that the sub-3 nm layer is not continuous across the TEM grid but shows significant fractures. Since these have been the initial attempts, a variety of possible reasons can account for this such as mechanical stress during the transfer or capillary forces acting when removing the sample from the Cu-etching solution. Nevertheless, substantial areas of the freestanding Pd/Cu layer are easily observed, thus, allowing for a detailed analysis. The image of Fig. 6a shows areas where structures with periodicities in the Angstrom range are clearly seen next to regions where no order is discernible. In addition, longer range periodicities are present, which can be assigned as Moiré patterns from the superposition of structures with different periodicities and/or orientations. The Fourier transform shown in the inset of Fig. 6a exhibits discrete spots appearing at different angles and k-values with some of them well-defined and others appearing diffuse in the azimuthal direction. This, on the one hand, indicates some variation in the azimuthal orientation but, on the other hand, suggests that the formation of crystalline structures is influenced by the underlying SAM. This is corroborated by the fact that the analysis of sub-10 nm areas well separated by several tens of nanometers yields spots within a narrow range of k-values which show the same orientation.

A quantitative evaluation of the k-values for different images gives a very low number of locations where dimensions fit well to the lattice parameters of bulk Pd and, thus, indicate the presence of Pd nanoparticles. An example is given in Fig. 6b which shows a magnification of area 4 marked in Fig. 6a. Analysis of the Fourier transform yields a value of 2.246 ± 0.05 Å which agrees very well with the (111) plane of Pd. As in this example, also in other spots we did not observe an orientation of Pd particles where the spots of the (200) plane showed up simultaneously to (111) spots at the expected angle of 55°. The only occasional occurrence of particles with bulk Pd dimensions might seem somewhat surprising considering that in the CCED process the formation of Pd particles is a prerequisite for Cu deposition. For the system studied here, which was performed in

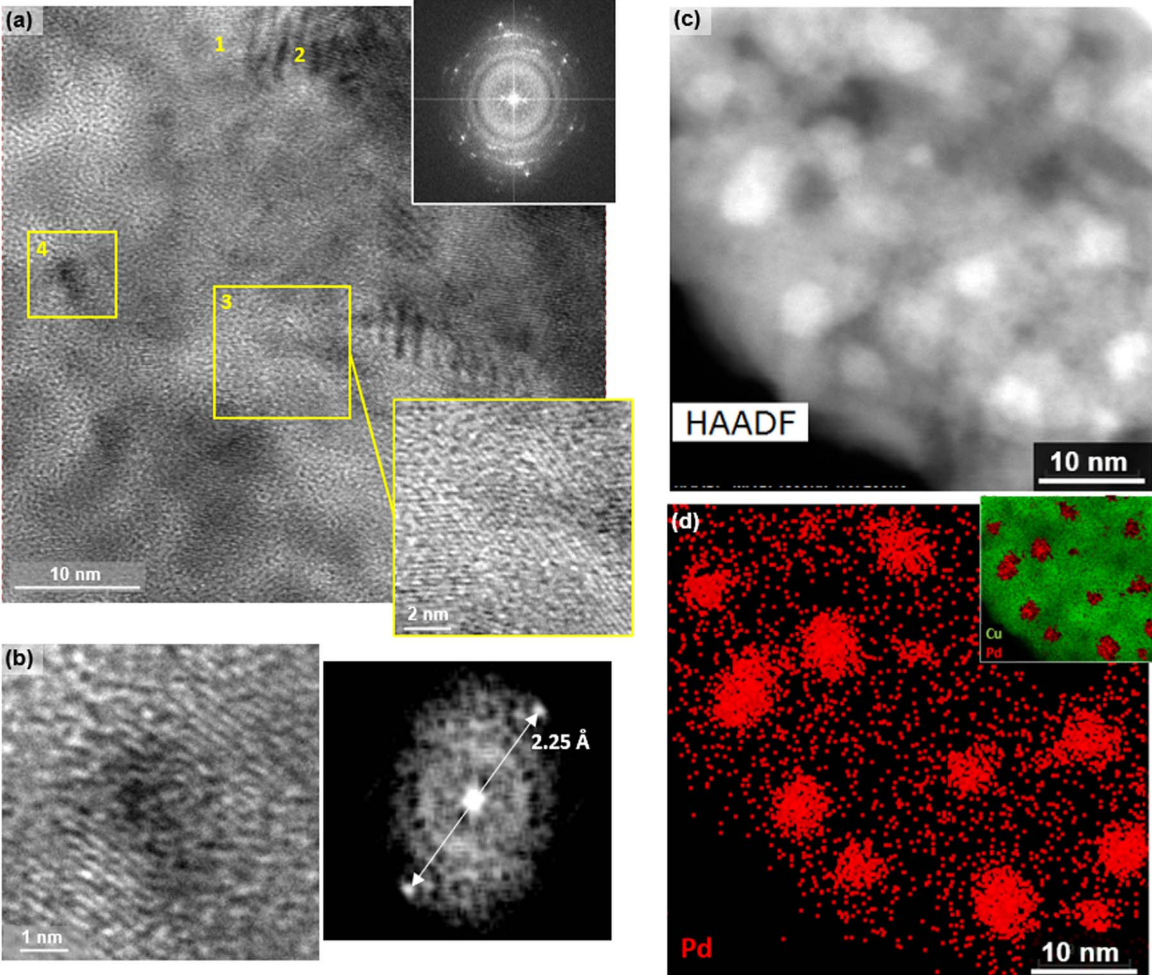

Figure 6. TEM images of a Pd/Cu layer prepared under the same conditions as described in Fig. 5. (a) Overview image with insets showing a magnified region of the layer and the Fourier transform of the full image. Areas marked 1–3 show regions of crystallinity mixed with areas where no order is discernible (b) High-resolution image of area 4 marked in (a). The corresponding Fourier transform yields a spacing of the lattice planes of 2.25 Å, the (111) plane of Pd. (c) HAADF-STEM image of Pd/Cu layer. (d) EDX maps of the same area as in (c) showing Pd in the main image and Cu in the inset with the Pd signal overlaid.

the presence of chloride as an accelerating additive (see Fig. 4f), it is likely that the size of the Pd core, in general, is so small that Pd structure is difficult to resolve, in particular since they are overgrown by an alloy with a different lattice constant. It will be interesting to compare the present results with layers prepared under different conditions where the Pd seed formation is more clearly separated from the Cu deposition.

In accord with the very fast onset of Cu deposition, values were more frequently observed which deviate from bulk Pd, and for both the (111) and (200) planes dimensions are observed in the range of 2.0–2.5 Å and 1.90–1.95 Å, respectively, which is consistent with the formation of the random A1 fcc phase of the Pd/Cu alloy[40,41] and a statistical variation of the Pd/Cu ratio. What is not clear at present is the observation of values in the range of up to 0.15 Å above the Pd bulk (111) and (200) values. Since other methods of Pd/Cu alloy synthesis are bulk-based and give rise to equilibrium structures, the question, open at this point, is whether the presence of the interface and the preparation under nonequilibrium conditions accounts for this by inducing strain.

For further elucidation of the composition of the Pd/Cu layer, the distribution of the elements was probed by HAADF and EDX. An image of the former is shown in Fig. 6c where the contrast variations indicate an inhomogeneous distribution of both elements. The sensitivity of HAADF imaging to atomic numbers ($Z_{Pd} = 46$, $Z_{Cu} = 29$) suggests that Pd is concentrated in the bright spots, which is confirmed by Fig. 6d showing the EDX map of Pd with most of it concentrated in particles 5–7 nm in diameter and 10–15 nm apart. In between these particles the concentration of Pd is rather uniform. The copper distribution shown in the inset of Fig. 6d is also rather uniform which indicates that the Pd/Cu alloy is not only present between particles but also covers the Pd nanoparticles. Looking at the variations in the size of the Pd particles and distance-dependent changes in the Pd concentration it is not surprising that the Pd/Cu alloy forms with a significantly varying Pd/Cu ratio which in turn affects the lattice dimensions,[41] in agreement with the analysis of the FT images. Summarising, the TEM images fully support the suggested mechanism outlined above and illustrated in Fig. 2 that the Pd nanoparticles generated by the 2-D deposition act as seeds for the Cu deposition. Once Cu deposition is enabled it overlaps with any further Pd reduction and diffusion at the SAM/electrolyte interface, thus resulting in the formation of the alloy.

Conclusions

Coordination-controlled electrodeposition of Pd/Cu on a highly ordered thiol monolayer terminated by a pyridine unit has been investigated. In contrast to defect-mediated deposition on electrodes modified by passivating SAMs, the molecule plays an active role in the process by selectively coordinating Pd^{2+} from an electrolyte containing both copper and palladium. This fundamentally changes the mechanism of bimetal deposition compared to conventional protocols due to the reduced dimensionality of the Pd deposition

from a 2-D layer of coordinated ions. Distinct features of the 2-D process are an accelerated nucleation, which enables the 3-D deposition of metal from the bulk electrolyte on top of the SAM, and the temporal overlap between the 2-D and the 3-D process, offering new prospects for alloy formation. Defect-mediated deposition as a parallel process can be eliminated provided the deposition parameters comprising deposition potential and time, metal concentration in the electrolyte and degree of metal coordination are properly chosen.

Through the number of complexation/reduction steps the deposition can be varied from isolated particles 3–10 nm in diameter to ultrathin continuous layers of 2–3 nm thickness. Lift-off of the latter has opened up new vistas for their nanoscopic characterization by TEM-based techniques and it will be of utmost interest to establish the correlation between the deposition parameters and the resulting structures. This will be crucial for the further development of the CCED scheme for bimetal deposition. One area of interest is catalysis[42] where the particular features of the CCED process such as the temporal overlap of the 2-D and 3-D process offer additional ways to tailor catalytic activity via composition and mesoscopic structure of the alloy. Another area is SAM-templated electrodeposition for the generation of metallic nanostructures.

The paradigm change from deposition mediated by defects in SAMs to one determined by the SAM molecules via complexation allows for a much better control of the nucleation process and thus of the dimensions of the deposits, including the generation of ultrathin layers. This combines favourably with the availability of techniques to pattern SAMs at high lateral resolution.[43,44]

Acknowledgments

Support by the Chinese Scholarship Council and the University of St Andrews for a stipend (Z. Y.) are gratefully acknowledged. Electron microscopy was carried out at the Electron Microscopy Facility, School of Chemistry, University of St Andrews and we acknowledge recent funding for the Facility from the EPSRC (EP/T019298/1, EP/L017008/1) and the EPSRC Strategic Resources Grant (EP/R023751/1).

Supporting Information

Supporting Information with additional STM images, and the description of the lift-off and transfer of the ultrathin Pd/Cu layers is available. The research data supporting this publication can be accessed at https://doi.org/10.17630/b047a584-c933-481e-ab71-be8c6d3e9097.

ORCID

Aaron B. Naden https://orcid.org/0000-0003-2876-6991
Richard T. Baker https://orcid.org/0000-0002-3304-3280
Manfred Buck https://orcid.org/0000-0003-1225-7607

References

1. P. L. Schilardi, O. Azzaroni, and R. C. Salvarezza, *Langmuir*, **17**, 2748 (2001).
2. T. Felgenhauer, C. Yan, W. Geyer, H. T. Rong, A. Gölzhäuser, and M. Buck, *Appl. Phys. Lett.*, **79**, 3323 (2001).
3. O. Azzaroni, P. L. Schilardi, and R. C. Salvarezza, *Electrochim. Acta*, **48**, 3107 (2003).
4. I. Thom, G. Hähner, and M. Buck, *Appl. Phys. Lett.*, **87**, 024101 (2005).
5. G. Pattanaik, W. Shao, N. Swami, and G. Zangari, *Langmuir*, **25**, 5031 (2009).
6. Z. She, A. DiFalco, G. Hähner, and M. Buck, *Beilst. J. Nanotechnol.*, **3**, 101 (2012).
7. Z. She, A. Di Falco, G. Hähner, and M. Buck, *Appl. Surf. Sci.*, **373**, 51 (2016).
8. T. Baunach, V. Ivanova, D. M. Kolb, H. G. Boyen, P. Ziemann, M. Buttner, and P. Oelhafen, *Adv. Mater.*, **16**, 2024 (2004).
9. V. Ivanova, T. Baunach, and D. M. Kolb, *Electrochim. Acta*, **50**, 4283 (2005).
10. J. A. Mwanda and A. Cuesta, *Curr. Opin. Electrochem.*, **17**, 72 (2019).
11. H. G. Boyen, P. Ziemann, U. Wiedwald, V. Ivanova, D. M. Kolb, S. Sakong, A. Gross, A. Romanyuk, M. Buttner, and P. Oelhafen, *Nature Mat.*, **5**, 394 (2006).
12. H. Müller, M. Metzler, N. Barth, B. Conings, H. G. Boyen, T. Jacob, and L. Kibler, *Electrocatalysis*, **9**, 505 (2018).
13. M. Saitner, F. Eberle, J. Baccus, M. D'Olieslaeger, P. Wagner, D. M. Kolb, and H. G. Boyen, *J. Phys. Chem. C*, **116**, 21810 (2012).
14. Z. Yao, M. Buck, and M. Bühl, *Chem. Eur. J.*, **26**, 10555 (2020).
15. J. A. Keith and T. Jacob, *Chem. Eur. J.*, **16**, 12381 (2010).
16. J. Kucera and A. Gross, *Phys. Chem. Chem. Phys.*, **14**, 2353 (2012).
17. F. Eberle, M. Saitner, H. G. Boyen, J. Kucera, A. Gross, A. Romanyuk, P. Oelhafen, M. D'Olieslaeger, M. Manolova, and D. M. Kolb, *Angew. Chem. Int. Ed.*, **49**, 341 (2010).
18. M. Piescheck, A. Abdelrahman, J. M. Hermann, H. Müller, T. Jacob, and L. A. Kibler, *Electrocatalysis*, **12**, 264 (2021).
19. J. Gajdzik, J. Lenz, H. Natter, R. Hempelmann, G.-W. Kohring, F. Giffhorn, M. Manolova, and D. M. Kolb, *Phys. Chem. Chem. Phys.*, **12**, 12604 (2010).
20. B. Luo, A. Banik, E. W. Bohannan, and J. A. Switzer, *J. Phys. Chem. C*, **124**, 21426 (2020).
21. Z. She, Z. Yao, H. Ménard, S. Tobish, D. Lahaye, N. R. Champness, and M. Buck, *Nanoscale*, **11**, 13773 (2019).
22. M. I. Muglali, J. Liu, A. Bashir, D. Borissov, M. Xu, Y. Wang, C. Wöll, and M. Rohwerder, *Phys. Chem. Chem. Phys.*, **14**, 4703 (2012).
23. M. I. Muglali, A. Bashir, A. Birkner, and M. Rohwerder, *J. Mater. Chem.*, **22**, 14337 (2012).
24. C. Silien, D. Lahaye, M. Caffio, R. Schaub, N. R. Champness, and M. Buck, *Langmuir*, **27**, 2567 (2011).
25. C. Silien, M. Buck, G. Goretzki, D. Lahaye, N. R. Champness, T. Weidner, and M. Zharnikov, *Langmuir*, **25**, 959 (2009).
26. I. Horcas, R. Fernandez, J. M. Gomez-Rodriguez, J. Colchero, J. Gomez-Herrero, and A. M. Baro, *Rev. Sci. Instrum.*, **78**, 013705 (2007).
27. C. A. Schneider, W. S. Rasband, and K. W. Eliceiri, *Nat. Methods*, **9**, 671 (2012).
28. J.-N. Chazalviel and P. Allongue, *J. Am. Chem. Soc.*, **133**, 762 (2011).
29. A. M. El-Aziz, L. A. Kibler, and D. M. Kolb, *Electrochem. Commun.*, **4**, 535 (2002).
30. C. T. J. Low, C. P. de Leon, and F. C. Walsh, *Trans. Inst. Met. Finish.*, **93**, 74 (2015).
31. D. M. Soares, S. Wasle, K. G. Weil, and K. Doblhofer, *J. Electroanal. Chem.*, **532**, 353 (2002).
32. W. Shao, G. Pattanaik, and G. Zangari, *J. Electrochem. Soc.*, **154**, D201 (2007).
33. Z. Nagy, J. P. Blaudeau, N. C. Hung, L. A. Curtiss, and D. J. Zurawski, *J. Electrochem. Soc.*, **142**, L87 (1995).
34. Y. I. Yanson and M. J. Rost, *Angew. Chem. Int. Ed.*, **52**, 2454 (2013).
35. W. Shao, G. Pattanaik, and G. Zangari, *J. Electrochem. Soc.*, **154**, D339 (2007).
36. K. Mech, P. Zabinski, R. Kowalik, and K. Fitzner, *J. Electrochem. Soc.*, **160**, H770 (2013).
37. N. Wattanavichean, M. Gilby, R. J. Nichols, and H. Arnolds, *Anal. Chem.*, **91**, 2644 (2019).
38. C. Silien and M. Buck, *J. Phys. Chem. C*, **112**, 3881 (2008).
39. O. Shekhah, C. Busse, A. Bashir, F. Turcu, X. Yin, P. Cyganik, A. Birkner, W. Schuhmann, and C. Wöll, *Phys. Chem. Chem. Phys.*, **8**, 3375 (2006).
40. X. Cai, A. Wang, J. Wang, R. Wang, S. Zhong, Y. Zhao, L. Wu, J. Chen, and S. Bai, *J. Mat. Chem. A*, **6**, 17444 (2018).
41. A. A. Popov, Y. V. Shubin, P. E. Plyusnin, M. R. Sharafutdinov, and S. V. Korenev, *J. Alloys Compd.*, **777**, 204 (2019).
42. M. Gholinejad, F. Khosravi, M. Afrasi, J. M. Sansano, and C. Nájera, *Catal. Sci. Technol.*, **11**, 2652 (2021).
43. W. Geyer, V. Stadler, W. Eck, M. Zharnikov, A. Gölzhäuser, and M. Grunze, *Appl. Phys. Lett.*, **75**, 2401 (1999).
44. C. Shen and M. Buck, *Nanotechnol.*, **20**, 245306 (2009).